



**HAL**  
open science

## Effects of nanofillers on morphology and surface wetting of microporous polypropylene composite membranes

Bicy K, Anu Paul P, Nandakumar Kalarikkal, Arul Manuel Stephen, Geethamma G, Didier Rouxel, Sabu Thomas

### ► To cite this version:

Bicy K, Anu Paul P, Nandakumar Kalarikkal, Arul Manuel Stephen, Geethamma G, et al.. Effects of nanofillers on morphology and surface wetting of microporous polypropylene composite membranes. Materials Chemistry and Physics, 2021, 257, pp.123742. 10.1016/j.matchemphys.2020.123742 . hal-03405792

HAL Id: hal-03405792

<https://hal.univ-lorraine.fr/hal-03405792v1>

Submitted on 26 Sep 2022

**HAL** is a multi-disciplinary open access archive for the deposit and dissemination of scientific research documents, whether they are published or not. The documents may come from teaching and research institutions in France or abroad, or from public or private research centers.

L'archive ouverte pluridisciplinaire **HAL**, est destinée au dépôt et à la diffusion de documents scientifiques de niveau recherche, publiés ou non, émanant des établissements d'enseignement et de recherche français ou étrangers, des laboratoires publics ou privés.

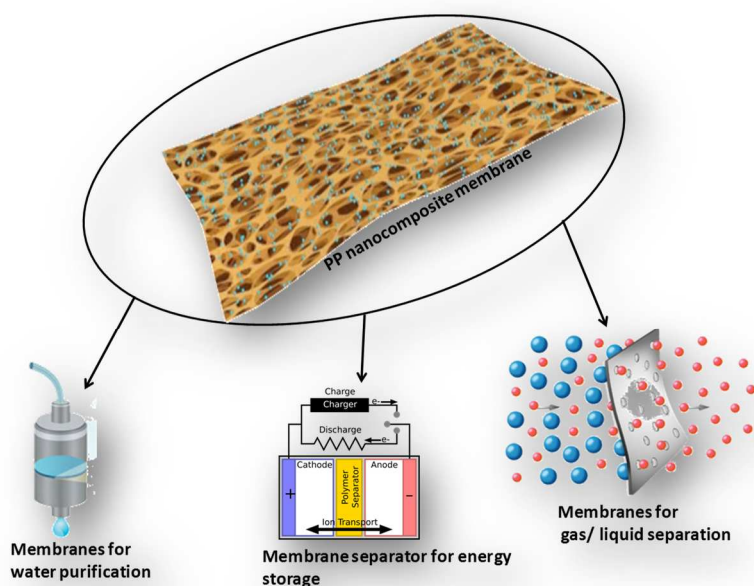


Distributed under a Creative Commons Attribution - NonCommercial 4.0 International License

## Effects of nanofillers on morphology and surface wetting of microporous polypropylene composite membranes

Bicy K<sup>1,2</sup>, Anu Paul P<sup>1</sup>, Nandakumar Kalarikkal<sup>1,3</sup>, Arul Manuel Stephen<sup>4</sup>, Geethamma V G<sup>1</sup>,  
Didier Rouxel<sup>2</sup>, Sabu Thomas<sup>1,2,5</sup>

1. International and Inter University Center for Nanoscience and Nanotechnology, Mahatma Gandhi University, Kottayam, India
2. Université de Lorraine, 54000 Vandoeuvre-Lès Nancy, France
3. School of Pure and Applied Physics, Mahatma Gandhi University, Kottayam, India
4. Central Electrochemical Research Institute, CSIR-CECRI, Karaikudi, Tamilnadu
5. School of Chemical Sciences, Mahatma Gandhi University, Kottayam, India



### Abstract:

Microporous polypropylene (PP) nanocomposite membranes suitable for various applications such as energy storage, water purification, membrane separation, etc., were prepared by melt mixing of polypropylene and natural rubber (NR) subsequently followed by etching of rubber phase. Nanoparticles having spherical shape ( $\text{Al}_2\text{O}_3$ ), irregular shape ( $\text{TiO}_2$ ), and 2D platelet morphology (Cloisite 30B (C-30B)), were used to the influence of nanoparticles on pore morphology and wetting properties of PP. Morphology of PP membrane was investigated by SEM and TEM analysis and the study reveals that all the prepared membranes possess a continuous porous structure with a minimum percentage porosity of  $62 \pm 2$ . Mechanical studies showed that the nanoparticles have a significant effect on tensile strength, strain to failure, and Young's modulus. DSC results indicate that the nanoparticles do not make any

significant change on the melting temperature of polypropylene. Polarized optical microscopic studies reveal that nanofillers enhances spherulite growth by acting as a heterogeneous nucleating agent. Contact angle measurements using two different test liquids (distilled water and Dimethyl sulfoxide (DMSO)), reveals that Al<sub>2</sub>O<sub>3</sub> added PP exhibits good wettability in both the test liquids. The present studies reveal that the shape, properties, and active surface area of the nanofillers greatly influence the morphological mechanical and wetting properties of microporous PP.

**Key Words:** Microporous; PP nanocomposites; 3D and 2D nanoparticles; morphology; wetting behavior.

## **Introduction**

The microporous polymer nanocomposites are widely employed in various fields such as water treatment, sensing applications, battery separators, proton exchange membranes, fuel cells, and gas-gas, liquid-liquid, liquid-solid separations<sup>1</sup>. The importance of porous polymer membrane is due to its straight forward pore-forming mechanism, high surface area, high flexibility, and low cost<sup>2</sup>. Porous polymer nanocomposite materials have gained much attention in recent years due to the hybrid properties of polymers and nanofillers<sup>3</sup>. In any composition, these materials offer unique mechanical, optical, and thermal properties. The nanofillers can be of any shape such as spherical, platelet, and rod-like, etc, and are used to improve the properties of the polymer matrix. Commonly used fillers are carbon black, carbon nanotubes, SiO<sub>2</sub><sup>4</sup>, metal oxides<sup>5-9</sup>, different types of clays (Montmorillonite, Cloisite 10A, 30B, 20A, etc)<sup>10</sup>, cellulose nanocrystals, nanofibers, quantum dots, etc. The property enhancement of the material depends on the nature of nanofillers, effective dispersion of the nanoparticles in the polymer matrix, size and shape of the nanofillers, the active surface area of the fillers in the polymer matrix, and interaction between the polymer matrix and the nanoparticles etc.

Various methods have been employed for the fabrication of porous polymeric membranes. Among them, electrospinning and solvent casting are commonly used. The solvent casting method offers good mechanical strength however low porosity of the membrane is one of the major drawbacks. Shawky et al. developed multi-wall carbon nanotube/ aromatic polyamide composite membranes through the polymer grafting process. The result showed that the well-dispersed multiwalled carbon nanotubes (MWCNTs) increased the membrane strength<sup>11</sup>. Porous polyvinylidene fluoride-trifluoro ethylene (P(VDF-TrFE)) membranes were prepared

by Costa et al. by the solvent evaporation method for lithium-ion battery separator application, and reported that the prepared membrane shows a percent porosity of 70-80<sup>12</sup>. Electrospun microporous nanofibrous membrane offers very high porosity (>80 %), but poor mechanical property limits its extensive applications. Dey et al. fabricated microporous P(VDF-TrFE) nanofibrous membranes by electrospinning for energy harvesting<sup>13</sup>. Poly(vinylidene fluoride) (PVDF)/clay electrospun nanofibrous membranes were prepared by Prince et al. for direct contact membrane distillation (DCMD) applications. The results show that the incorporation of clay increases the hydrophobicity of the membrane and the clay particles influence the crystallization process of the nanocomposite membrane<sup>14</sup>. Phase inversion technique is another method used to prepare microporous membranes. The foremost advantage of this method is that one can tune the porosity of the membrane and also these membranes offers good mechanical stability. Prasanth et al. prepared hybrid organic–inorganic polymer gel electrolytes (PGEs) based on polymer–clay nanocomposite microporous membrane separators for lithium ion battery by phase inversion method. The authors reported that incorporation of nano-clay in PGE enhances its ionic conductivity, provides high charge–discharge capacity and shows stable cycle performance<sup>15</sup>. Koh et al. prepared polyvinylidene fluoride-hexafluoropropylene (PVDF-HFP) / clay nanocomposite membranes by phase inversion method, with increased membrane modulus and porosity<sup>16</sup>. Bae et al. synthesized fouling-resistant nanocomposite membranes via electrostatic self-assembly between TiO<sub>2</sub> nanoparticles and sulfonic acid groups on the membrane surface. Phase inversion method is used for the preparation of porous nanocomposites<sup>17</sup>. polyvinylidene fluoride membranes modified by alumina nanoparticles was synthesized by Li et al. and was used to purify oily wastewater from an oil field. Authors also reported that the addition of nanosized alumina particles improves the membrane antifouling performance and the flux recovery ratio<sup>18</sup>. Blending of polymers and etching one of the components from the blend is another method for the fabrication of porous membranes. Bose et al. prepared porous PE membranes by etching PEO from PE/PEO blend, and these membranes were used for water purification<sup>19</sup>. Subramania and coworkers fabricated PVdF-co-HFP-ZrO<sub>2</sub>based composite micro-porous polymer electrolyte separator for lithium ion battery, by a preferential polymer dissolution process. This novel membrane showed higher ionic conductivity and discharge capacity<sup>20</sup>. Melt mixing and preferential etching is one of the components from the polymer blend is a novel method for the fabrication of microporous membranes. Porosity and pore size depend on the dispersion and percentage composition of

the etched component, so one can tune the porosity and pore size by proper selection of polymers and also by varying the percentage composition of the polymers

The main objective of the present study is to develop microporous polypropylene nanocomposite membranes and to study the effect of size and shape of nanofillers on morphology, mechanical, thermal and wetting properties of PP. Fabrication of microporous PP nanocomposite membranes by selective extraction of one of the blend component is not reported elsewhere. All the reported work of PP nanocomposite studied the influence of nanofillers loading on morphological, mechanical, thermal and other properties of PP, and there is no reported work which compares and study the effect of nanofillers on morphology mechanical and wetting properties of microporous PP. The present work gives insight in to the pore morphology and tuning the pore structure by selecting proper nanofillers and blend ratio. Natural rubber (NR) and polypropylene (PP) are selected for the preparation of microporous membranes. Both the polymers are low cost and PP is well known for its excellent properties such as low density, thermal stability, chemical inertness, transparency, mechanical strength and stretchability. Three different nanofillers were selected for the study. One is Cloisite 30B (C-30B) having 2D platelet morphology, the second one is nano  $\text{Al}_2\text{O}_3$  having Spherical morphology with average particle size 5-10 nm. The third one is nano  $\text{TiO}_2$  having irregular shape with average particle size 21nm. Composites were prepared by melt-mixing method and the membranes were made porous by etching the rubber phase from the composites.

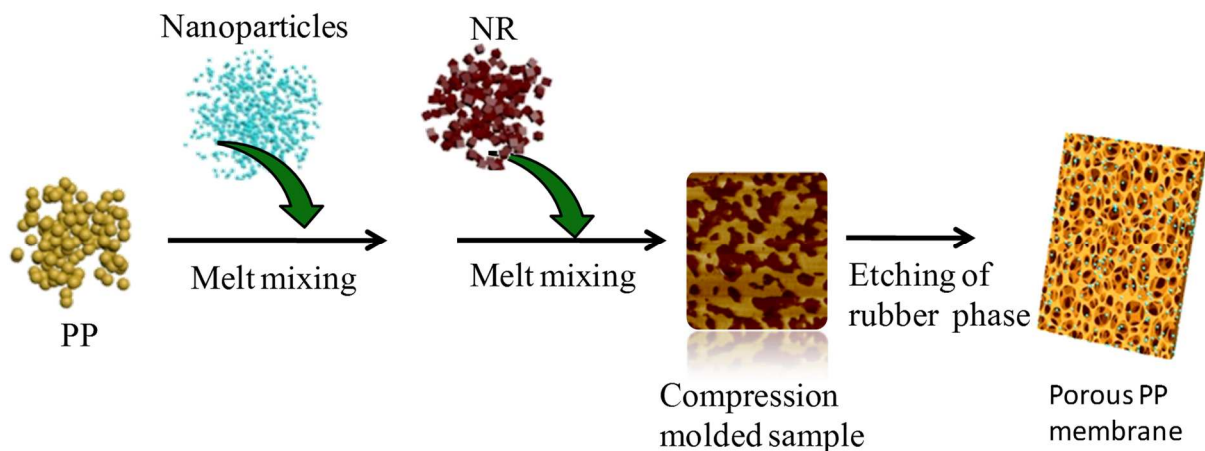
## **Materials and methods**

The polypropylene (PP), isotactic homopolymer with the commercial name repol (H350FG) used in this study was supplied by Reliance Industries Limited, India, with average molecular weight  $\sim 5,30,000$  g/mol. The natural rubber (NR) ISNR-5 with a density of  $0.97$  g/cm<sup>3</sup>, weight average molecular weight  $\sim 7,80,000$  g/mol, was supplied by Rubber Research Institute India (RRII) Kottayam, Kerala, India. The organically modified hydrophobic nanoclay, Cloisite (C-30B), was obtained from Southern Clay Products. Hygroscopic  $\text{Al}_2\text{O}_3$  (average particle size  $< 10$  nm,) and  $\text{TiO}_2$  (average particle size 21nm and mostly in anatase phase) nanopowder were obtained from Sigma Aldrich.

### **Preparation of NR/PP membranes**

The PP/NR nanocomposites were prepared by melt mixing in a Brabender Plasticorder. Prior to the mixing, PP and the nanoparticles ( $\text{Al}_2\text{O}_3$ , C-30B and  $\text{TiO}_2$ ) were dried in vacuum at 80 °C for 6 h. For efficient mixing of the blend components, the high viscosity of NR was reduced by masticating NR for 5 min in a two-roll mill mixer. PP was melted in the Brabender for 2 min and then nanoparticles were added and mixed for 3 min. Subsequently the NR was added and mixed for 5 more min. The processing parameters were fixed as the following: temperature of mixing 180 °C, screw speed at 60 rpm and mixing time 10 min. The processed materials were granulated and the samples were made in to thin film (50-60  $\mu\text{m}$ ) by compression molding at 180 °C for 5 min. Three different nanoparticles were used for the preparation of nanocomposites (NR/PP/ $\text{Al}_2\text{O}_3$ , NR/PP/C-30B and NR/PP/ $\text{TiO}_2$ )

The compression molded thin sheet of PP-NR nanocomposites were immersed in toluene in a beaker, and the solvent was refilled on the second day. After three days entire rubber particles were found to be dissolved in the solvent and the membrane became microporous. Four different types of membranes (50% NR etched PP, 50% NR etched PP with 4%  $\text{Al}_2\text{O}_3$ , C-30B and  $\text{TiO}_2$ ) having different porosity were obtained. These membranes were dried in an air oven at 110 °C for 6 h in order to remove the last traces of toluene if any.



Scheme 1. Preparation of microporous PP nanocomposite membrane

### Characterization techniques

Morphology of the microporous polypropylene nanocomposites was studied by Scanning electron microscope (GEOL -SEM 6390). The samples were sputtered using gold prior to analysis, in order to make the material conducting. The distribution of nanoparticles in the polymer matrix was studied by using High-Resolution Transmission Electron

Microscope (HR-TEM) (GEOL-JEM-3010). Co-continuity of the rubber phase in NR/PP blend was calculated by extracting the rubber phase in toluene. Two samples of each nanocomposite (NR/PP, NR/PP/Al<sub>2</sub>O<sub>3</sub>, NR/PP/C-30B and NR/PP/TiO<sub>2</sub>) were cut into 2 cm x 2 cm pieces and immersed in toluene for etching the rubber phase from the composite. Then the samples were dried in an oven at 100°C in order to remove traces of toluene and measured the weight of dry sample. Again, the samples were immersed in fresh toluene after measuring its dry weight; the process was repeated until there is no change in weight. Co-continuity index was calculated from the weight of samples before and after extraction using the equation,

$$\text{Co-continuity index } \phi_i = \frac{w_{1i} - w_{2i}}{w_{1i}} \quad (1)$$

where  $w_{1i}$  and  $w_{2i}$  are the weights of the component  $i$  (rubber) before and after extraction.

Mechanical properties of the membranes were studied using Universal testing machine Tinius Olesan (ASTM-D-638 method- strain from position). 10cmx1cm pieces of the samples were used and the testing was performed at a crosshead speed of 10 mm/min. A minimum of 5 samples were analyzed and the average was taken. Thermal transitions of the materials were studied by using Perkin Elmer Diamond DSC. About 2.25 mg of samples were heated from 50 ° to 200 ° C at a heating rate of 10 °C/ min under inert atmosphere, and the crystallization behavior of each sample was studied by cooling from 200 ° to 50 ° C. Percentage crystallinity of the membranes were calculated using the equation<sup>21</sup>,

$$\% X_c = \left( \frac{\Delta H_m}{\Delta H_m^0 (1 - \text{wt} \% \text{ Nps})} \right) \times 100 \quad (2)$$

where  $\Delta H_m$  is the enthalpy of fusion of the polymer,  $\Delta H_m^0$  is the standard enthalpy of fusion of 100% crystalline polymer, wt% Nps is the weight percentage of nanoparticles in the PP matrix. Enthalpy of fusion of 100% crystalline PP was taken as 165 J/g<sup>22</sup>, used to calculate the percentage crystallinity of copolymer. The lamellar thickness of the polymer was measured by using Gibbs-Thomson equation<sup>23</sup>,

$$T_m = T_m^o \left[ 1 - \frac{2\sigma_e}{\Delta H_m^o T_m^o L_c} \right] \quad (3)$$

where  $\Delta H_m^0$  is the standard enthalpy of fusion of 100% crystalline polymer,  $T_m^0$  is the equilibrium melting temperature of 100% crystalline polymer,  $L_c$  is the lamellar thickness and  $\sigma_e$  is the surface free energy of the polymer.

X-ray diffraction study was performed by using D8 Advance apparatus commercialized by Bruker. It is equipped with a germanium monochromator that produces Cu K $\alpha$ 1 radiation ( $\lambda = 0.154$  nm). the crystallinity of PP was calculated using the equation,

$$\text{Crystallinity} = \left( \frac{I(\text{Crystal})}{I(\text{Crystal}) + I(\text{Amorphous})} \right) \quad (4)$$

The influence of nanofillers on the crystallinity of PP was studied by observing the spherulite morphology using Leica DMLC polarized optical microscope. The samples were heated up to 180 °C for complete melting, and then cooled to 125 °C and the spherulite growth was observed in isothermal condition. The interactions between the nanofillers and the polymer were studied by FT-IR measurements and were performed in a shimadzu 1S series spectrometer.

The percentage porosity of the samples was measured by immersing 1cm x1cm samples in different liquids (DMSO, and n-butanol). After 24 Hrs, the sample is taken out and the excess liquid on the surface of the sample is removed and its weight is noted (wet weight). The weight of the sample before immersing in to the liquid (dry weight) was also measured. From the dry weight and wet weight, the percentage porosity was calculated using the equation<sup>24</sup>,

$$\text{Percentage of Porosity (P \%)} = \frac{M_l / \rho_l}{(M_l / \rho_l + M_p / \rho_p)} \times 100 \quad (5)$$

where  $M_l$  and  $M_p$  are the mass of the absorbed liquid and polymer,  $\rho_l$  and  $\rho_p$  are the densities of the liquid and polymer. The percentage porosity was measured using two different liquids (DMSO and n- butanol). The wettability behavior of the membranes in water and DMSO, was studied using Contact Angle Analyzer, SEO-Phoenix 300 from Surface

Electro Optics Co. Ltd, Korea. 1 am x1cm pieces of samples were used for the study and liquid drop was added to the sample surface using a micro syringe of drop volume 5  $\mu$ l. The contact angle readings were taken within 60 seconds of the addition liquid drop. Measurement was repeated six to eight times for each sample in order to get a precise and accurate result.

### Theory and calculation of contact angle results

The surface free energy of a solid ( $\gamma_s$ ) and a liquid that is in contact with the solid ( $\gamma_l$ ), interfacial free energy between solid and liquid ( $\gamma_{sl}$ ) and contact angle ( $\theta$ ) is related by Young equation<sup>25</sup>,

$$(\gamma_l) \cos(\theta) = (\gamma_s) - (\gamma_{sl}) \quad (6)$$

In the above equation ( $\gamma_s$ ) and ( $\gamma_{sl}$ ) are not amenable to direct measurement. Many approaches have been made by various scientists in order to obtain ( $\gamma_s$ ), however a satisfactory approach was made by Wu's. In order to verify Wu's approach; two liquids of dissimilar polarity- water and DMSO were selected for obtaining ( $\gamma_s$ ) of polymers.<sup>26</sup> Wu's harmonic mean equation for water and DMSO are given by the equation,

For water,

$$(1 + \cos(\theta_w))\gamma_w = \left[ \frac{\gamma_w^d \gamma_s^d}{\gamma_w^d + \gamma_s^d} + \frac{\gamma_w^p \gamma_s^p}{\gamma_w^p + \gamma_s^p} \right] \quad (7)$$

For DMSO,

$$(1 + \cos(\theta_d))\gamma_d = \left[ \frac{\gamma_d^d \gamma_s^d}{\gamma_d^d + \gamma_s^d} + \frac{\gamma_d^p \gamma_s^p}{\gamma_d^p + \gamma_s^p} \right] \quad (8)$$

where d and p are the contribution due to dispersion and polar forces. The total surface free energy is the energy associated with interface between two phases and it is a measure of intermolecular forces<sup>27</sup>. According to Owen's-Wendt theory, the total surface energy of a solid is,

$$\gamma_s = \gamma_s^d + \gamma_s^p \quad (9)$$

The Work of adhesion ( $W_A$ ) is the energy required to remove the liquid drop from the solid surface, which is calculated by the equation,

$$W_A = (1 + \cos \theta)\gamma_l \quad (10)$$

where  $\gamma_l$  is the surface tension of the liquid used for contact angle studies.

Interfacial energy is the energy necessary to form a unit area of the new interface in the system. It is always less than the sum of the separate surface energies of the two phases.

Dupres equation is used to find interfacial energy.

$$\gamma_{sl} = \gamma_s + \gamma_l - W_A \quad (11)$$

Spreading coefficient gives the idea about the wetting and spreading of a liquid on the surface of a solid. Positive value of spreading coefficient indicates spontaneous wetting and spreading of the liquid on the surface of a solid, and negative value indicates poor wetting. It also depends on the surface tension of the test liquid; a liquid with high surface tension would not spread much. Spreading coefficient is calculated by the equation,

$$S_c = \gamma_s - \gamma_{sl} - \gamma_l \quad (12)$$

Interaction parameter: The degree of interaction between the test liquid and solid polymer surface was studied by calculating Girifalco-Good's interaction parameter. A higher value of interaction parameter indicates greater interaction<sup>27</sup>.

$$\phi = \left[ \frac{\gamma_l(1 + \cos \theta)}{2(\gamma_l\gamma_s)^{1/2}} \right] \quad (13)$$

## Results and discussion

### 1. Morphological analysis – (SEM and TEM)

Scanning electron microscopic images of rubber etched PP nanocomposites are shown in Figure 1.  $a_1$ ,  $a_2$  and  $a_3$  are the SEM images of 50% NR etched PP, the pore morphology reveals that the NR is uniformly dispersed in PP. Co-continuous porous morphology was observed in all the membranes and the size and shape of the pores varies with the nature of nanofillers; this reveals that the dispersion of NR in PP is influenced by the nature of nanofillers. The addition of Cloisite 30B (C-30B) elongates the pore structure; this may be because of the platelet morphology of the clay particles. Spherical nanoparticles ( $Al_2O_3$  and  $TiO_2$ ) incorporated composite exhibits large pores with slightly spherical and co-continuous morphology. The average pore size was calculated by using Image J software, it was observed that the pore width increases with the addition of nanofillers; neat membrane showed an average pore width of 0.90 micrometer, whereas C-30B,  $TiO_2$  and  $Al_2O_3$  showed an average pore diameter of 1.03, 1.46 and 1.57 micrometer respectively. The nanoparticles are visible in the SEM images  $b_3$  and  $d_3$ ; this concludes that the nanoparticles are present in PP matrix and interphase. It is confirmed from the report of Jarnthong et al. that on premixing the nanoparticles with PP before blending with NR, the majority of nanoparticles remains in the PP phase and interface. The nanoparticles coated with molten PP disperse the nanoparticles within the PP matrix<sup>28-31</sup>. The lower complex viscosity of PP compared to NR also helps the nanoparticles to remain in the PP phase.

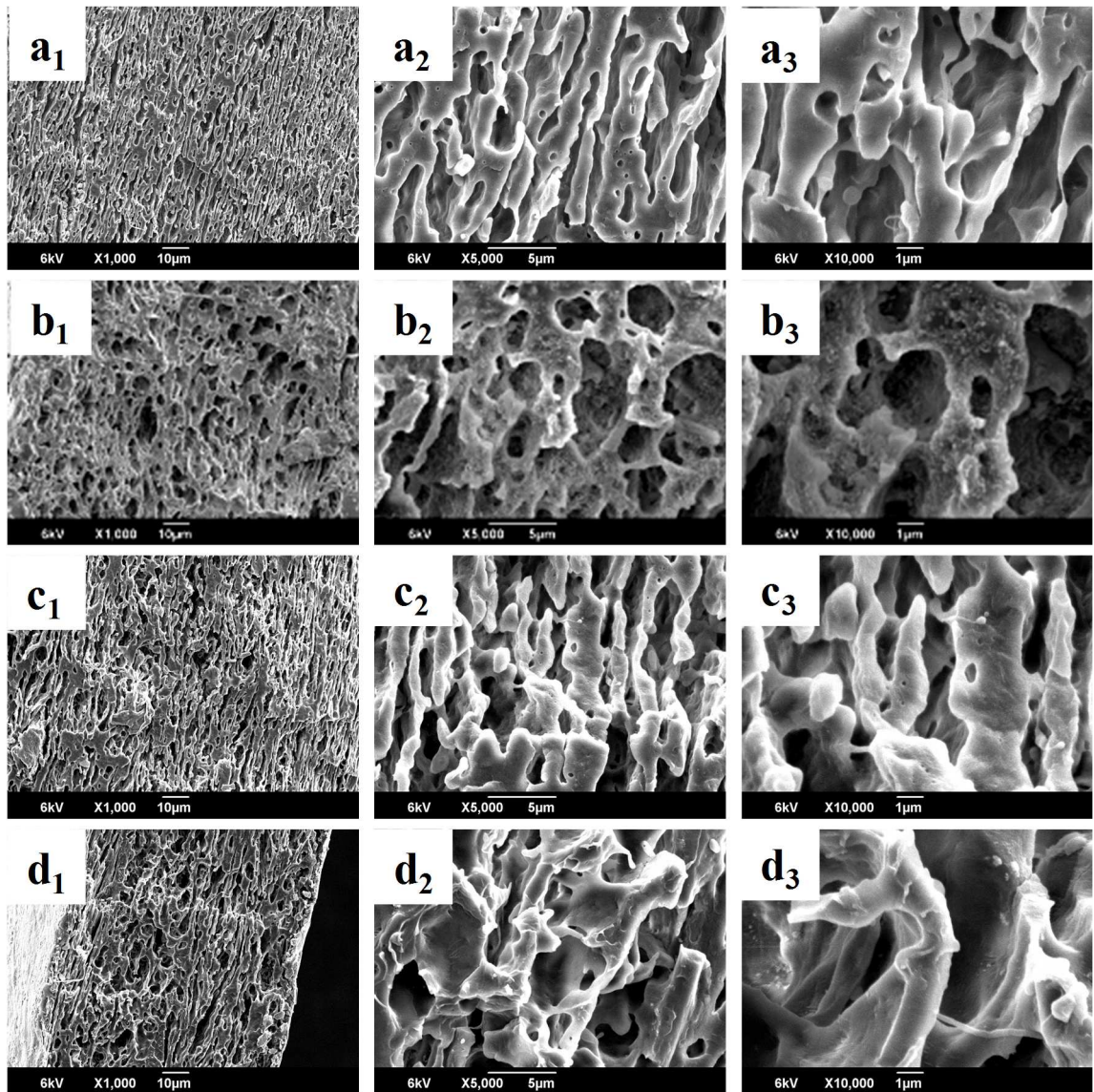


Figure 1. SEM images of 50% NR etched PP, (a<sub>1</sub>-a<sub>3</sub>) neat PP, (b<sub>1</sub>-b<sub>3</sub>) PP/ Al<sub>2</sub>O<sub>3</sub>, (c<sub>1</sub>-c<sub>3</sub>) PP/ C-30B, and (d<sub>1</sub>-d<sub>3</sub>) PP/TiO<sub>2</sub> with different magnifications.

The dispersion of fillers in the polymer nanocomposite was observed through Transmission electron microscope (TEM). Figure 2. represents the transmission electron microscopic images of PP nanocomposites, the HR-TEM images were taken before extracting the NR phase in order to study the localization of nanoparticles. Two phases, one dark and one bright phase can be observed in the TEM image. A dark phase represents high absorption and bright phase represents lower absorption. The high cohesive energy density and crystallinity of PP prevents the transmission of large number of electrons through it and therefore PP appears as dark, whereas NR allows the transmission of electrons because of its low cohesive

energy density and amorphous nature, therefore it appears as bright phase. The clay particles are partially intercalated and exfoliated in the nanocomposite and TEM image shows that clay particles are located at the PP phase. The average particle size of  $\text{Al}_2\text{O}_3$  and  $\text{TiO}_2$  was calculated from the TEM image and it was found to be approximately 7.0 nm and 31.0 nm, however it exists as agglomerates in the polymer matrix. TEM image clearly shows that  $\text{TiO}_2$  nanoparticle forms bigger agglomerates compared to  $\text{Al}_2\text{O}_3$ , this reduces the interaction with polymer chain. TEM image also shows that nanofillers are mainly localized at the PP phase. The TEM images of nanoparticle shows that the nanoparticle exists in agglomerated form and the agglomeration is slightly increased in the PP nanocomposite. Tem image also reveals that the clay platelets partially exfoliated in the PP matrix.

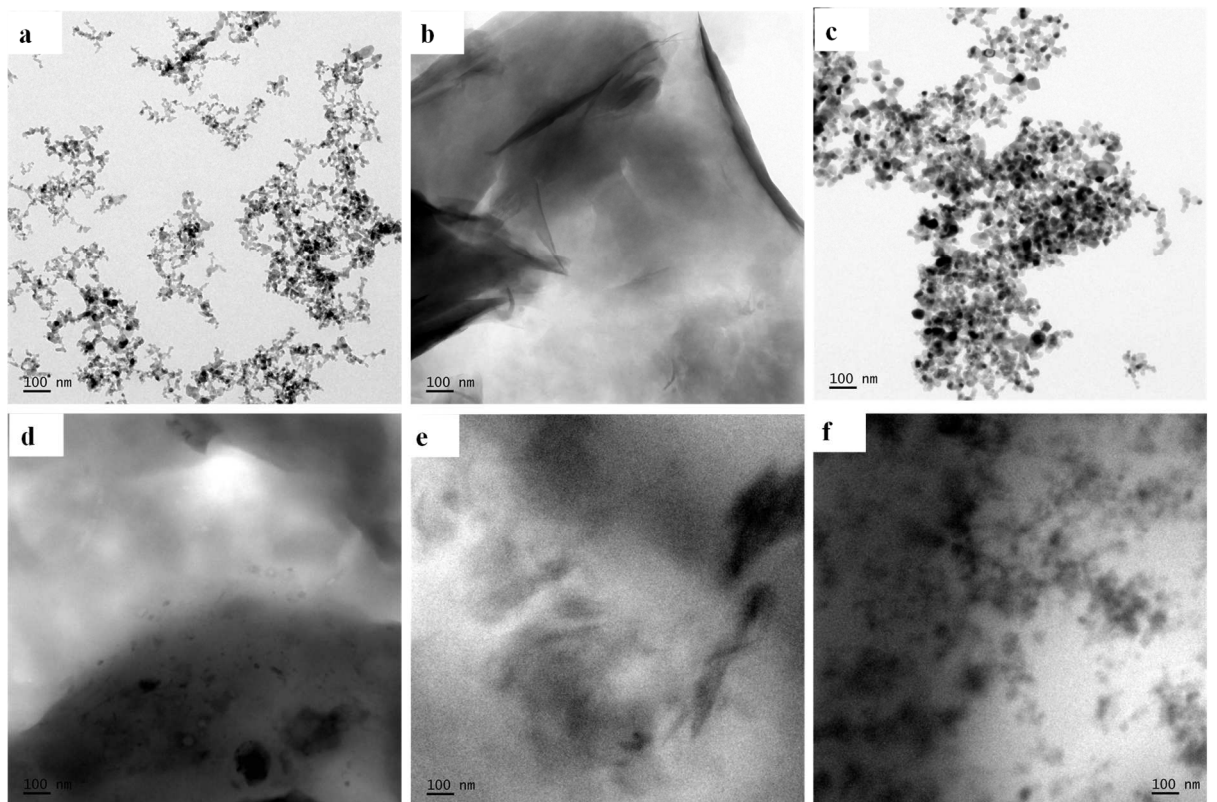


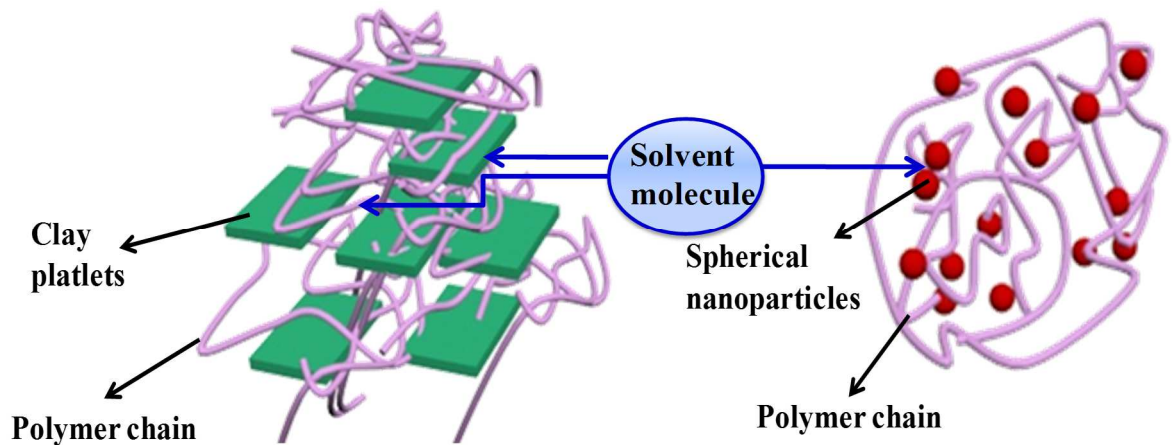
Figure 2. TEM images of, a)  $\text{Al}_2\text{O}_3$  b) C-30B, c)  $\text{TiO}_2$ , d) PP/C-30B, e) PP/C-  $\text{Al}_2\text{O}_3$ , and f) PP/  $\text{TiO}_2$ .

## 2. Co-continuity index and percentage porosity

Co-continuous porous morphology of the membranes was observed through SEM analysis. It was further confirmed by calculating co-continuity index (eq.1). The co-continuity indexes of the rubber etched PP membranes are listed in Table 1. Co-continuity index is influenced by various factors such as interfacial tension, viscosity ratio, processing condition filler dispersion etc. Rubber etched neat PP shows a co-continuity index of 0.92. The lower co-continuity index of nanocomposite is due to the presence of nanoparticles, which hinder the penetration of solvent molecules into the system. Co-continuity index also varies with the nature, size and shape of the nanoparticles. The lowest co-continuity index is shown by Al<sub>2</sub>O<sub>3</sub> added system; may be due to the viscosity enhancement effect of the nanoparticles. Nanofillers mainly goes to the low viscous PP component, which enhances the viscosity of PP matrix and also act as an obstruction for the effective etching of rubber phase<sup>32</sup>. The interaction of polymer with spherical and platelet nanoparticles is shown in scheme 2. This interaction prevents the easy penetration of solvent molecules and effective etching of the rubber phase and this is responsible for the slight reduction in porosity and co-continuity index of nanocomposites. The percentage porosity of the microporous PP nanocomposite membranes was calculated using equation (4), all the prepared membranes shows a percentage porosity in the range of 62 to 65. The addition of nanoparticles slightly reduces the percentage porosity of PP membrane.

Table 1. Co-continuity index of 50% NR etched PP nanocomposites

Sample	Weight of rubber before extraction	Weight of rubber after extraction	Co – Continuity index	Percentage porosity
Neat PP	0.2524	0.0187	0.9259±0.002	65±2
PP/Al <sub>2</sub> O <sub>3</sub>	0.0876	0.008	0.9086 ±0.001	62±2
PP/C-30B	0.3657	0.0305	0.9165±0.003	64±2
PP/TiO <sub>2</sub>	0.1883	0.0157	0.9166±0.002	63±2



Scheme 2. Nanoparticle dispersion in PP matrix and solvent penetration

### 3. Mechanical properties

Mechanical studies of the microporous PP Nanocomposite membranes are shown in Figure 3. (a, b and c). In the stress-strain plot (a), all the nanocomposite membranes have superior mechanical properties than neat PP. However, a small reduction in stress is observed in case of  $\text{Al}_2\text{O}_3$  added PP, this is may be due to the agglomeration of nanoparticles. C-30B(clay) added PP exhibits highest tensile strength of 6.6 MPa and modulus of 194.5, due to the intercalation and exfoliation of clay platelets. The polymer chains are entered and confined in to the intergallery spacing of layered silicates and separates the layers. This enhances the Van der Waals interaction of clay platelets with PP matrix and thereby increases the modulus. The intercalated geometries of C-30B in the PP matrix act as a crack preventing as well as load bearing agent<sup>33,34</sup>.  $\text{Al}_2\text{O}_3$  added PP also shows high modulus of 182.5 MPa. The strong interfacial interaction of  $\text{Al}_2\text{O}_3$  and PP matrix helps effective load transfer, which intensify the tensile modulus<sup>35</sup>.  $\text{TiO}_2$  added PP shows a small decrease in tensile modulus. This may be due the agglomeration of  $\text{TiO}_2$  nanoparticle, which reduces the contact area between the filler and polymer matrix and leads to poor dispersion and low tensile modulus<sup>36,37</sup>. Elongation at break increases with the addition of nanoparticles,  $\text{TiO}_2$  added PP shows a strain % of 20.19. This is because of the shear yielding of the polymer prior to the formation of crazes<sup>38</sup>. The high elongation of the PP nanocomposite reveals the uniform dispersion of nanoparticles on the polymer matrix. The well dispersed nanoparticles help to transfer the stress throughout the composite and are responsible for the toughening of the nanocomposite systems. Tensile strength, elongation at break and Young's modulus of PP nanocomposites is listed in Table 2.

Table 2. Mechanical properties of 50% NR etched PP nanocomposites

Sample	Tensile Strength (MPa)	% Elongation	Young's Modulus (MPa)
Neat PP	4.7	8.4	125.0± 10.4
PP/Al <sub>2</sub> O <sub>3</sub>	4.4	11.6	182.5± 5.8
PP/C-30B	6.6	16.5	194.5± 8.4
PP/TiO <sub>2</sub>	4.9	20.1	123.2± 4.1

Figure 3. Mechanical properties of 50% NR etched PP nanocomposites, a) Stress-Strain curve, b) and c) variation of tensile strength and modulus as a function of filler type.

Figure 3. Mechanical properties of 50% NR etched PP nanocomposites, a) Stress-Strain curve, b) and c) variation of tensile strength and modulus as a function of filler type.

#### 4. Thermal studies – DSC

Figure 4. shows the DSC heating scan and cooling scan of PP nanocomposites; neat PP melts at 161.11 °C and nanoparticles slightly decreases the melting temperature of PP. In the DSC thermogram, it was found that a sub-endothermic peak appears in the melting curve of nanocomposites. The exact reason for the formation of sub-endothermic peak is not known, however it is believed that this is due to the formation of imperfect crystals<sup>35</sup>. The sub-endothermic peak is prominent in case of Al<sub>2</sub>O<sub>3</sub>, which melts at 158.°C. crystallisation temperature (T<sub>c</sub>), melting temperature (T<sub>m</sub>),



Neat PP	116±1	161±1	52.46	33.1	3.6	4.5	5.9
PP/Al <sub>2</sub> O <sub>3</sub>	116±1	158±1	47.15	29.8	3.5	4.1	5.9
PP/C-30B	117±1	160±1	53.49	33.7	3.5	4.4	6.5
PP/TiO <sub>2</sub>	117±1	161±1	58.11	36.7	3.6	4.5	6.5

## 5. X-ray diffraction (XRD) studies

Figure 5 represents the X-ray diffractograms of PP nanocomposite and nanoparticles,  $2\theta$  at  $14.2^\circ$  (110),  $17.6^\circ$  (040),  $18.6^\circ$  (130),  $22.0^\circ$  (111),  $25.6^\circ$  (060) and  $28.7^\circ$  (220) are the characteristic peaks of  $\alpha$ - crystalline forms of PP and a small peak observed at  $21.2^\circ$  (301) is the  $\beta$  crystalline structure of PP. XRD studies prove that PP mainly exists in  $\alpha$ - crystalline structure. Compared to neat PP, no distinctive difference in the  $2\theta$  angle is found for PP nanocomposite. This indicates that nanoparticle does not change the crystal form of PP. Nanocomposite shows a reduction in the peak intensity, and this indicates that nanoparticle shows that structural changes brought about with polymer interaction and intercalation<sup>42</sup>. XRD spectrum of Al<sub>2</sub>O<sub>3</sub> nanoparticle shows peaks at  $32.2^\circ$ ,  $36.4^\circ$ ,  $45.5^\circ$ ,  $66.9^\circ$  and TiO<sub>2</sub> nanoparticle exhibit a sharp peak at  $25.5^\circ$  which indicates that TiO<sub>2</sub> is in anatase phase<sup>43</sup>. C-30B shows a peak at  $4.7^\circ$ , the characteristic peak of cloisite 30B. The XRD spectrum of PP/Al<sub>2</sub>O<sub>3</sub> and PP/TiO<sub>2</sub> exhibit similar behavior and PP/C-30B shows a dramatic decrease in the peak intensity of PP indicating that the clay platelets are exfoliated in the PP matrix. The peak at  $4.7^\circ$  is absent in the nanocomposite, it also evidences for the exfoliation of clay platelets. The lowest peak intensity of clay filled PP is attributed to the increased surface area of clay platelets and intercalation of polymer chains in the clay gallery<sup>44</sup>. The crystallinity was measured from the X-ray diffraction pattern by calculating the area under the peak. The crystallinity was evaluated using the equation 4<sup>45</sup>. The crystallinity values are tabulated in Table 4. The study conclude that the nanofillers do not change the crystallinity of the polymer but the shape and surface area of the nanofillers influence the orientation of polymer chains in different crystal planes.

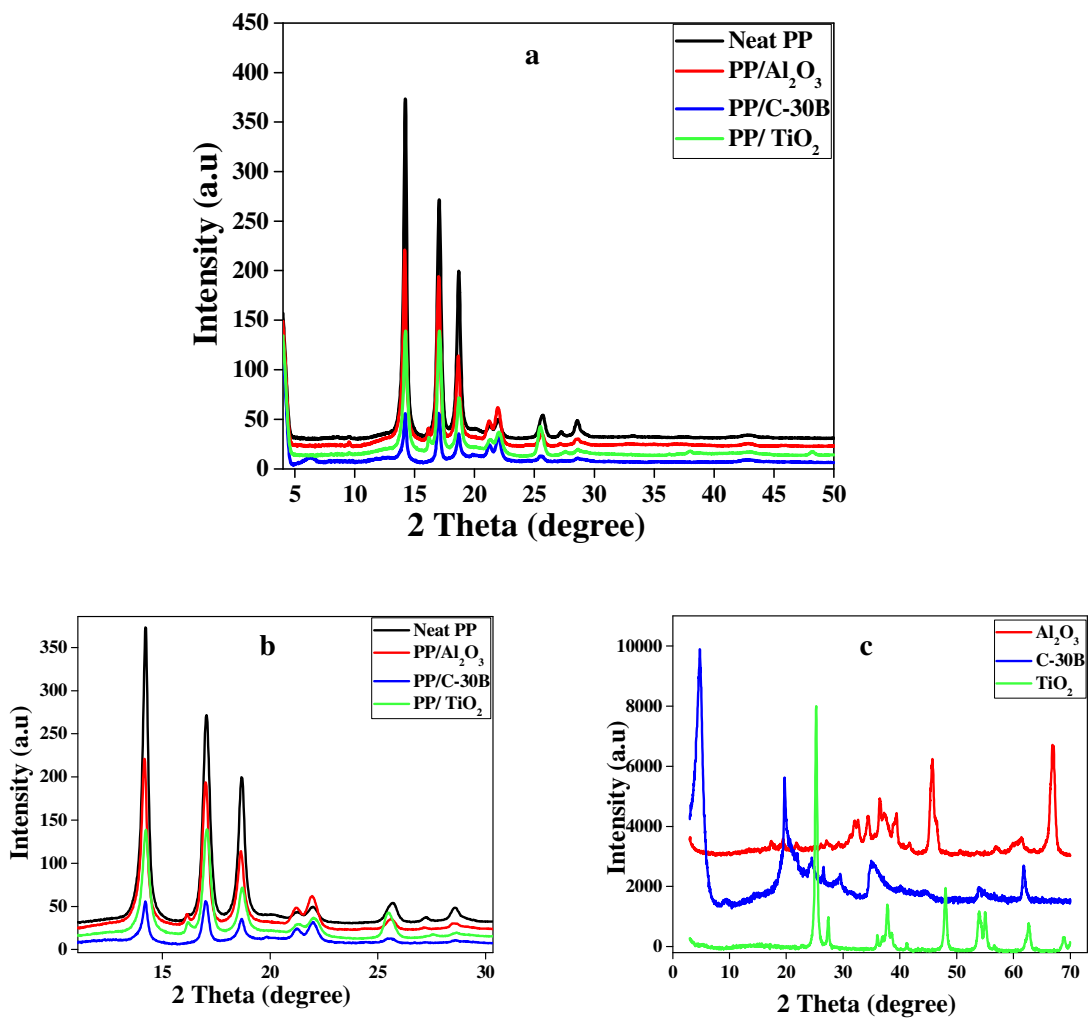


Figure 5. X-ray diffractograms of a) 50% NR etched PP nanocomposites, b) magnified peaks in the  $2\theta$  region  $10^\circ$ - $30^\circ$ , c) XRD pattern of nanoparticles

Table 4. The crystallinity of PP calculated from XRD

Sample	Crystallinity (XRD)

Neat PP	47.4
PP/Al <sub>2</sub> O <sub>3</sub>	36.8
PP/C-30B	44.0
PP/TiO <sub>2</sub>	45.7

## 6. Optical studies

Polarized optical microscopic images of neat PP and PP nanocomposites are shown in Figure 6. The incorporation of nanoparticles reduces the spherulite size of PP, this is evidence for the nucleating effect of nanoparticles<sup>46</sup>. Figure 5a is the optical microscopic image of neat PP. Incorporation of Al<sub>2</sub>O<sub>3</sub> (Figure 5b) reduces the rate of crystallization and bigger spherulites are formed. This indicates that Al<sub>2</sub>O<sub>3</sub> nanoparticle does not encourage crystal growth by acting as a heterogeneous nucleating agent. The spherulite size of the C-30B system is similar to neat PP and TiO<sub>2</sub> (Figure 5d) added PP, a large number of small crystals are observed. This indicates that TiO<sub>2</sub> nanoparticles slightly initiate crystallization by acting as a site for spherulite growth. Large numbers of crystals generated were very close to each other. When the boundaries of the crystals are in contact, their growth impedes, resulting in a dramatic decrease in spherulite size<sup>35</sup>.

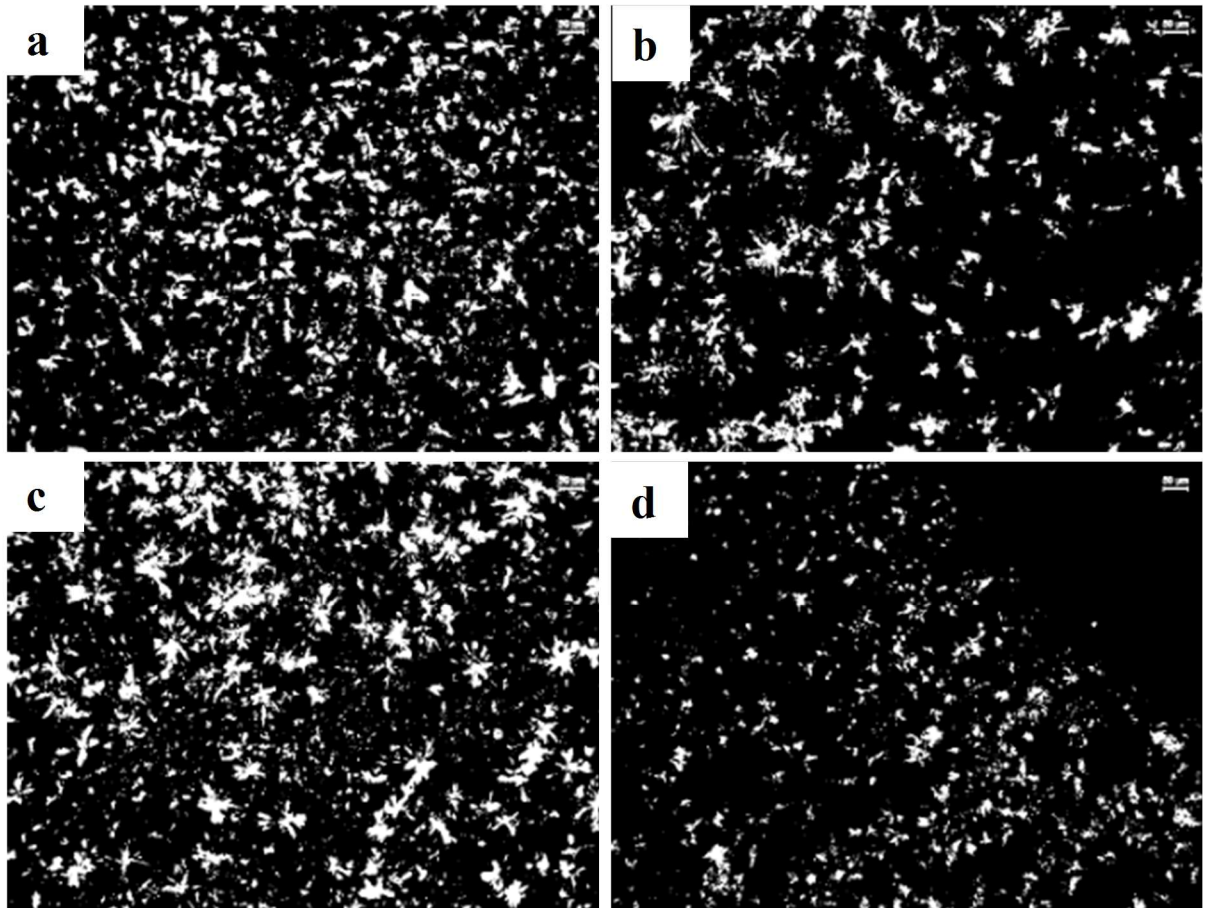


Figure 6. Polarized optical microscopic images of 50% NR etched PP nanocomposites, a) Neat PP, b) PP/Al<sub>2</sub>O<sub>3</sub>, c) PP/C-30B, d) PP/TiO<sub>2</sub>

#### 7. Fourier- transform infrared studies

Figure 7. represents the FT-IR spectra of NR etched PP nanocomposites. All the major peaks (2956, 2920, 2841, 1450, 1370, 1162, and 974 cm<sup>-1</sup>) in the spectra, indicate the isotactic nature of the polymer. The peaks at 2956 cm<sup>-1</sup> and 2920 cm<sup>-1</sup> are due to the symmetric stretching vibrations of -CH<sub>3</sub> and -CH<sub>2</sub>. On the other hand, the peaks at 1450 cm<sup>-1</sup> and 1381 cm<sup>-1</sup> are due to the symmetric and asymmetric scissoring vibrations of the CH<sub>3</sub> group. The peaks at 2920 and 2841 cm<sup>-1</sup> indicate the CH<sub>3</sub> symmetric stretching vibrations<sup>47</sup>. The bands at 1162, 974, and 840 cm<sup>-1</sup>, represent the helical chain of isotactic polypropylene. The amount of crystallinity is gauged by the presence of helical peaks. This is because the crystallites are formed over helical chains<sup>48,49</sup>. A weak band at 1096 cm<sup>-1</sup> in the PP/Al<sub>2</sub>O<sub>3</sub> spectrum indicates the Al-O-Al bond vibration and in PP/C-30B spectrum the weak band at 1099 cm<sup>-1</sup> is due to the Si-O-Si linkage of layered silicate<sup>50-52</sup>. The peak at 3427 cm<sup>-1</sup> shows the H-bonded O-H stretching; this may be due to the moisture present in the composite. There is no new peak arises or any shift in the peak position in the spectra of composite,

indicating that there is no specific chemical interaction between the filler and the polymer. The interaction between the nanoparticle and filler is the only physical force of attraction (Van der Waals interaction)

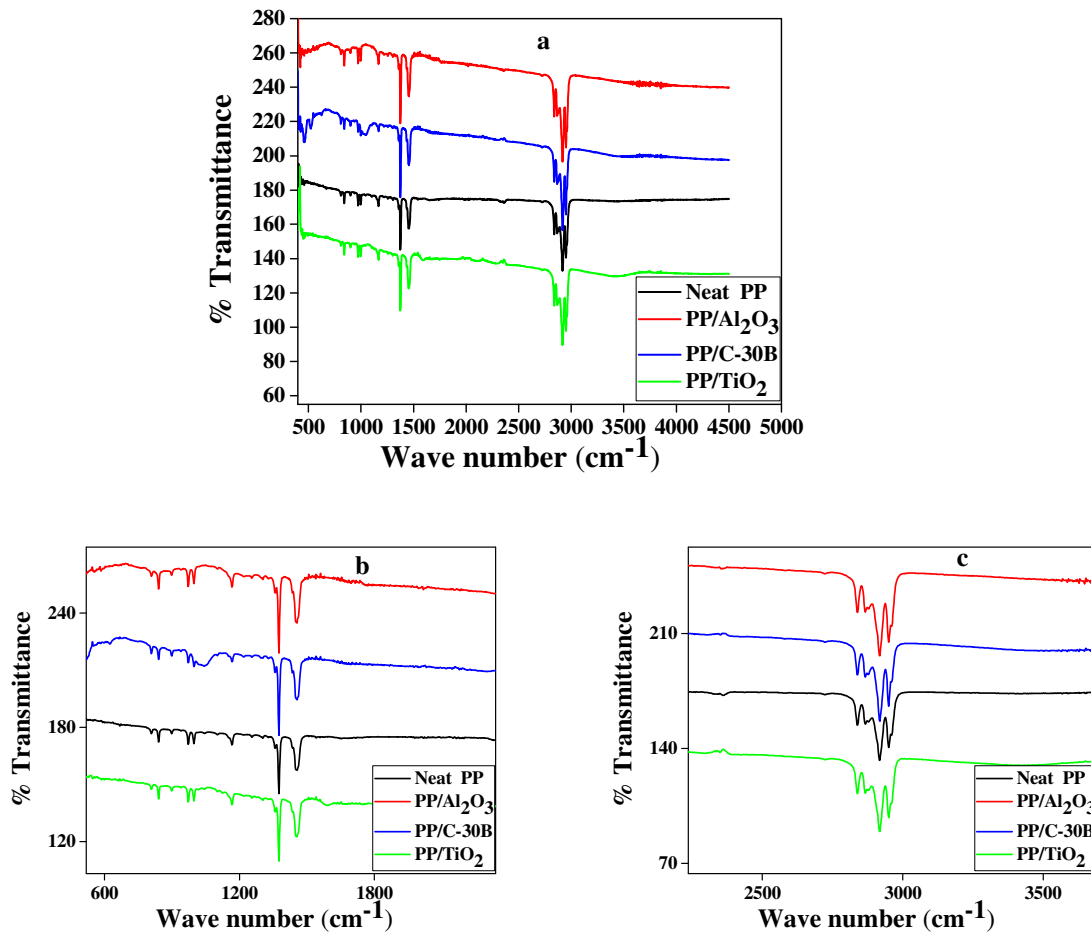


Figure 7. FT-IR spectra of a) 50% NR etched PP, b) magnified peaks in the 600-1800 cm<sup>-1</sup>, and c) magnified peaks in the 2000-3500 cm<sup>-1</sup> of NR etched PP nanocomposites

## 8. Contact angle analysis

The wetting behavior of microporous PP nanocomposite membranes was studied by contact angle analysis using two different test liquids such as water and DMSO. To analyze the wettability of PP nanocomposite membranes in the presence of a highly polar and less polar solvent, water and DMSO are selected. Contact angle values are influenced by various parameters such as the nature of the polymer, nature of the filler, surface roughness, and porosity of the sample material. In the present work, nanofillers such as Al<sub>2</sub>O<sub>3</sub>, TiO<sub>2</sub>, and C-30B, having a different shape (3D spherical and 2D platelet) and properties are used; also, in

all the samples, the nanofillers concentration was constant (4 wt %). The water contact angle and DMSO contact angle images of the microporous PP nanocomposite are shown in Figure 8.

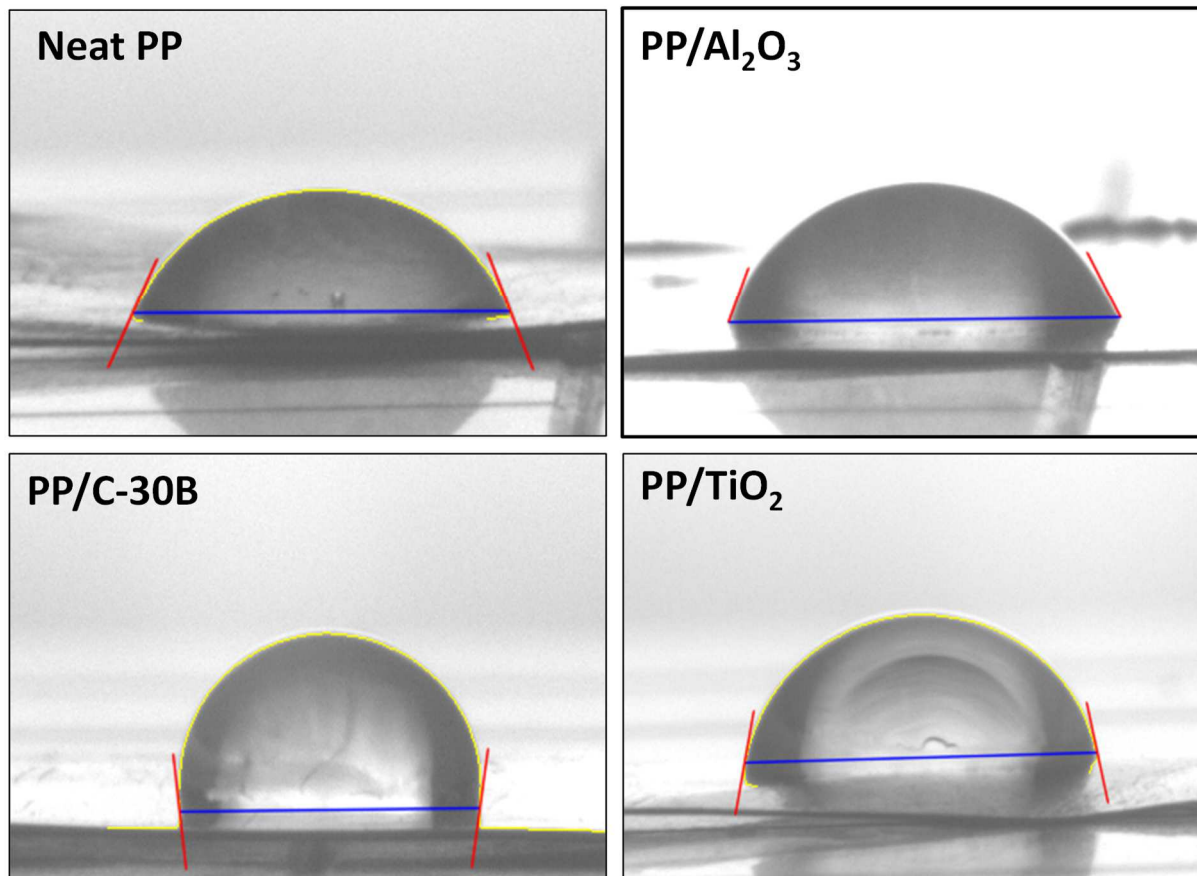


Figure 8a) Water contact angle of NR etched PP nanocomposites

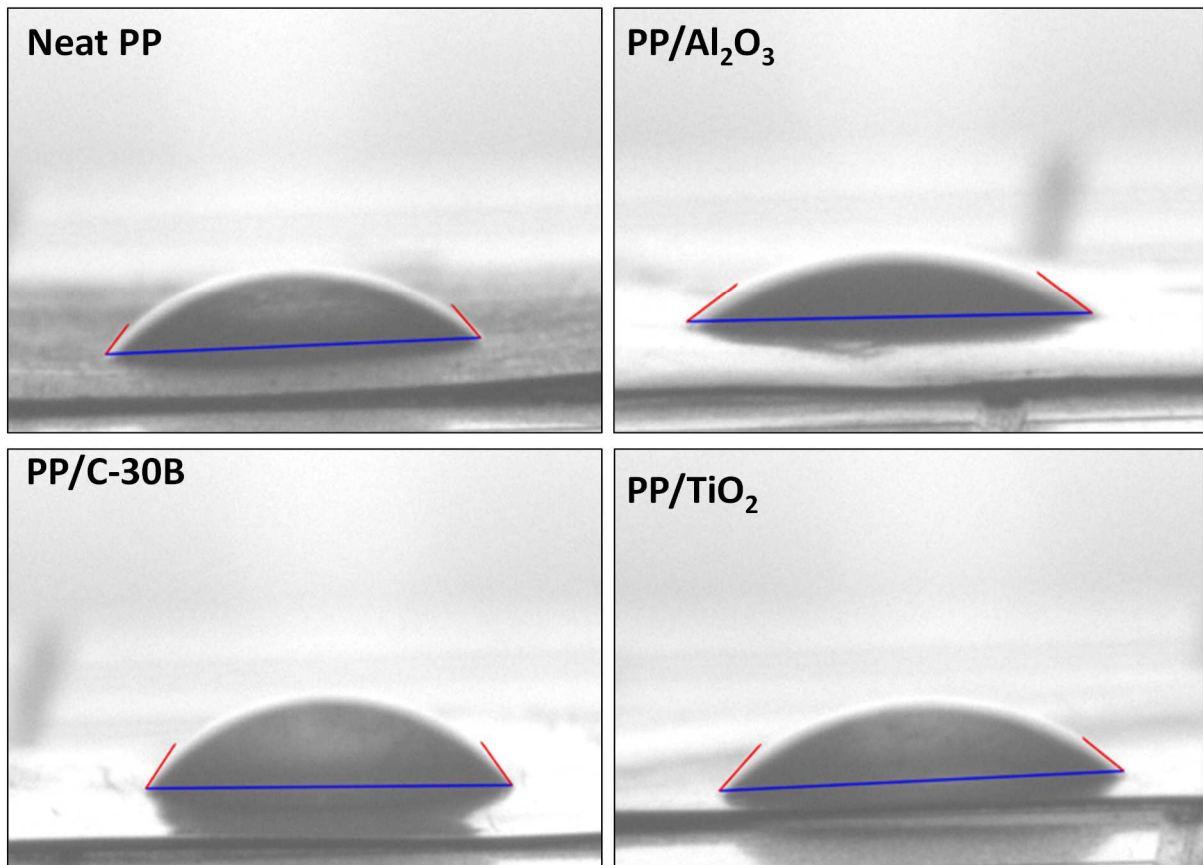


Figure 8b) DMSO contact angle of NR etched PP nanocomposites

Microporous PP shows a water contact angle of 66 °. The non-polar PP has little affinity towards the water; the low contact angle is because of its co-continuous porous morphology. The hygroscopic Al<sub>2</sub>O<sub>3</sub> nanoparticles interact with polar water molecules by making hydrogen bonds and decrease the contact angle of nonpolar PP to 63°<sup>53</sup>. SEM image also supports this observation. From the SEM image, it is clear that the nanoparticles are located at the PP matrix and interphase, which is responsible for the reduced contact angle. TiO<sub>2</sub> and C-30B added systems show a higher contact angle than PP. The spherical nanoparticles generally show higher contact angle values, this is because of their large surface area, in addition to this, it is clear from the TEM image that TiO<sub>2</sub> nanoparticle exists in the agglomerated form, which enhances the surface roughness. As a result of this also contact angle increases. The hydrophobic clay (C-30B) increases the nonpolar nature of PP and the exfoliated clay platelets in the polymer matrix reduce the co-continuous nature of the pores and increase the contact angle by increasing the repulsion between the nonpolar polymer and polar solvent<sup>26,54</sup>. DMSO shows a contact angle lower than that of water because of its less

polar nature. The contact angle of DMSO follows the same trend as that of the water contact angle, the lowest contact angle is observed for Al<sub>2</sub>O<sub>3</sub> added nanocomposite and the highest contact angle is shown by C-30B. The contact angle values of different nanofillers in water and DMSO systems are shown in Figure 9a.

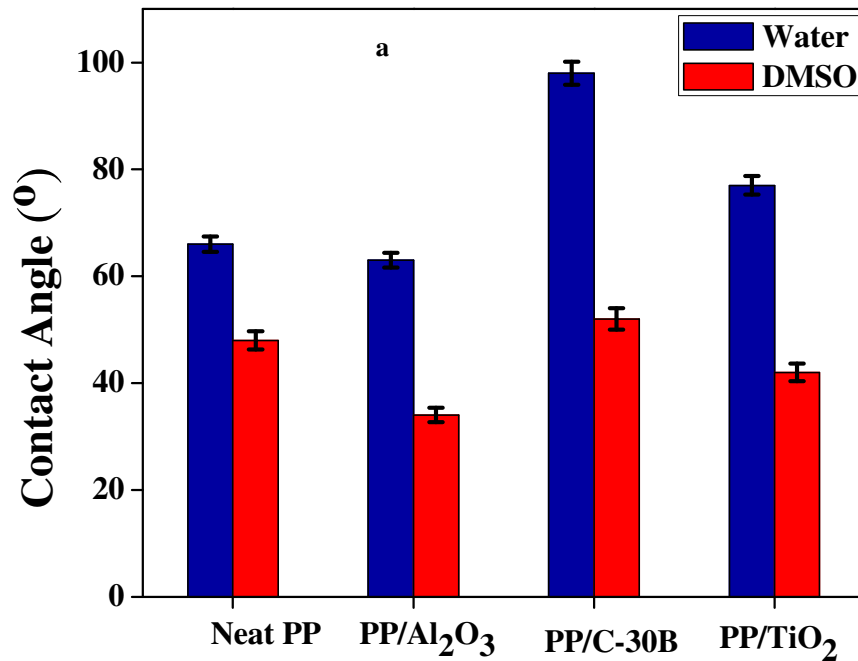


Figure 9a) Contact angle of NR etched PP nanocomposites with water and DMSO as the solvent

Polar-nonpolar interactions, polar-polar interactions, hydrogen bonding, van der Waal's interaction, porous morphology, surface roughness, etc. contribute towards polymer-solvent interactions. The work of adhesion, surface energy, spreading coefficient, and wetting energy also varies with contact angle. The work of adhesion depends on the surface tension of the liquid and contact angle. The work of adhesion of water and DMSO system is shown in Figure 9b. The small value of work of adhesion is a sign of poor interfacial bonding. In both water and DMSO, the lowest work of adhesion is shown by C-30B added PP; indicating poor interfacial interaction between clay and water, because of the hydrophobic nature of clay. Effective dispersion of the filler also increases the contact angle by enhancing the non-polar nature of the polymer, which will result in the reduced work of adhesion.

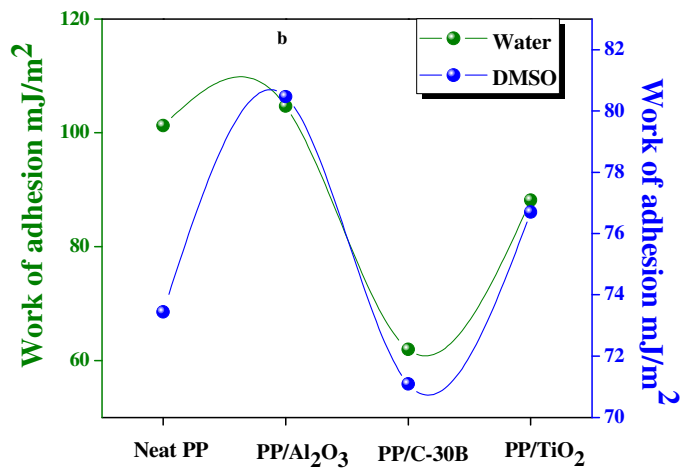


Figure 9b) Work of adhesion of NR etched PP nanocomposites with different fillers using water and DMSO as the solvent

Figure 9c. represents the interfacial energy of PP nanocomposites. The interface is a region of high energy compared to the bulk, and to maintain the lowest total energy of the system, the surface rearranges its configuration to minimize the excess energy. Interfacial energy between the two phases is low compared to the sum of their surface energies<sup>55</sup>. The interfacial energy of the water system is higher than DMSO. The increased interfacial energy indicates that there is less possibility of chemical attraction between the polymer surface and test liquid. The attraction between the sample and test liquid may be polar-polar, polar- non-polar, H- bonding, Van der Waals forces, etc. For the water-PP nanocomposite system, the possible attraction is H- bonding, and in the case of DMSO-PP, polar- nonpolar interaction is responsible for the increased interfacial energy. The low interfacial energy of Al<sub>2</sub>O<sub>3</sub> filled PP and water is because of the formation of H-bond between Al<sub>2</sub>O<sub>3</sub> and polar water. The high interfacial energy of PP/C-30B and water indicate the poor interaction between hydrophobic clay and water.

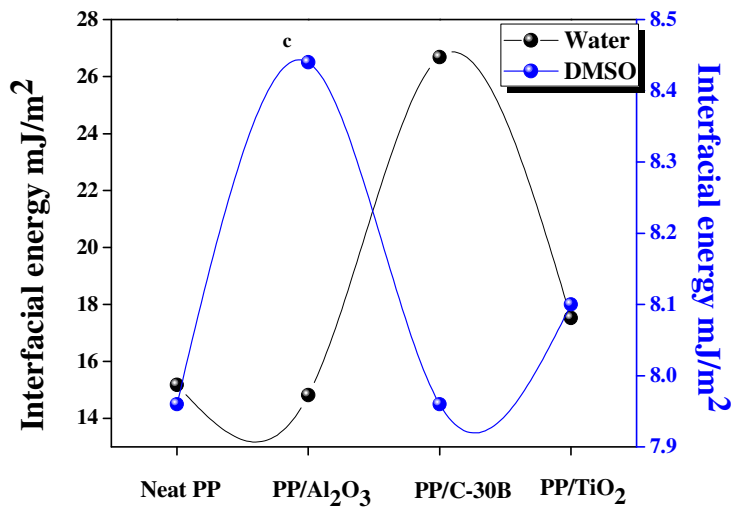


Figure 9c) Interfacial energy of NR etched PP nanocomposites with different fillers using water and DMSO as the solvent

The spreading coefficient indicates the spontaneous wetting and spreading of the test liquid on the solid surface. A positive value of the spreading coefficient represents good wetting and negative value shows poor wetting. Figure 9d represents the spreading coefficient of PP nanocomposites. Both water and DMSO show a negative value, however, the spreading coefficient of DMSO higher than water indicates that DMSO favors spreading and wetting. Among all the nanocomposites Al<sub>2</sub>O<sub>3</sub> shows the highest wetting and C-30B shows the least wetting in both water and DMSO. This proves that the presence of hygroscopic filler enhances the wetting and hydrophobic filler reduces the wetting property of the polymer.

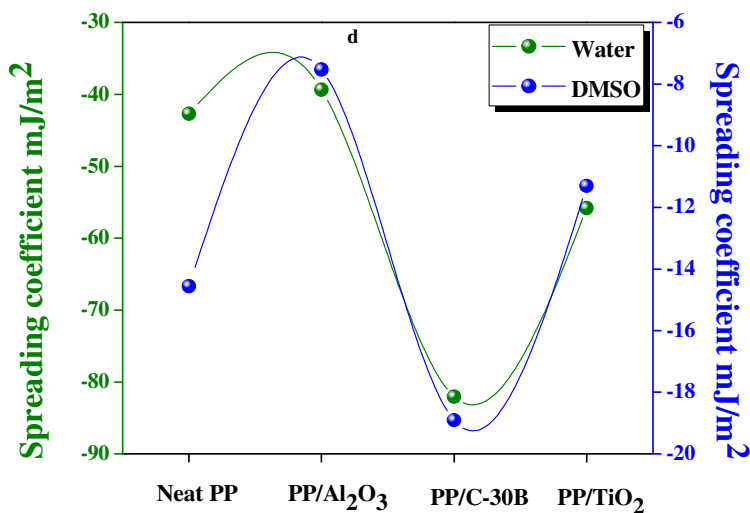


Figure 9d) Spreading coefficient of NR etched PP nanocomposite with different fillers using water and DMSO as the solvent

Girifalco- Good's interaction parameter is calculated using equation (10) and the results are shown in Figure 9e. The value of the interaction parameter changes from 0.5 to 1.5 and the Skapski type approach is used<sup>53</sup>. In this, all the interactions except the nearest neighborhood interactions are neglected. A higher interaction parameter indicates good interaction between the sample and the test liquid.  $\phi_w$  and  $\phi_d$  are the Girifalco- Good's interaction parameter due to water and DMSO respectively. Compared to water, DMSO shows a slightly higher value of the interaction parameter.

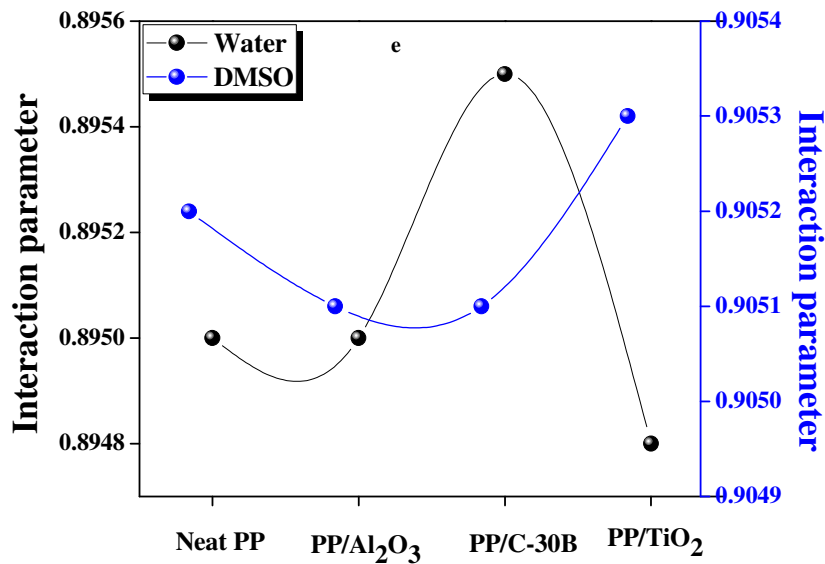


Figure 9e) Interaction parameter of NR etched PP nanocomposites using water and DMSO

## Conclusions

Microporous PP nanocomposite membranes were successfully prepared by melt mixing and solvent etching technique. Nanoparticles of different shapes (Al<sub>2</sub>O<sub>3</sub> and TiO<sub>2</sub> spherical and C-30B 2D platelet) and properties were used for the preparation of nanocomposites. In all the composites the concentration of the nanofillers was constant (4 wt %) and the properties of PP nanocomposites were compared. Morphological studies showed that the shape of nanoparticles influences the dispersion of rubber. C-30B added system shows elongated pore structure whereas Al<sub>2</sub>O<sub>3</sub> and TiO<sub>2</sub> system shows spherical shaped pores and all the

membranes show a minimum percentage porosity of 62. Nanofillers enhance the mechanical properties of PP; among the nanofillers, C-30B exhibits the highest tensile strength of 6.6 MPa and modulus of 194.5 MPa. The incorporation of nanofillers does not cause any significant change in the melting temperature of PP; however, the % crystallinity slightly varies depending on the nature of nanofillers. Optical microscopic studies show that crystal growth is affected by the nature of filler. FT-IR results indicate that there is no specific chemical interaction between the PP and nanofillers. Wetting behavior observed from contact angle analysis indicates that the contact angle of PP mainly depends on the nature of nanofillers. The highest wettability (contact angle 34°) was shown by Al<sub>2</sub>O<sub>3</sub> due to its hygroscopic nature and the lowest wettability was observed in the case of hydrophobic C-30B added systems. PP nanocomposite membranes show low contact angle and good interaction, with less polar DMSO compared to polar water. The calculated Girifalco Good's interaction parameter also confirms that PP has good interaction with less polar DMSO, than with water.

### **Acknowledgment**

The authors are gratefully acknowledged for the financial support given by the Council of Scientific and Industrial Research (CSIR), New Delhi.

### **References**

1. Jadav, G. L. & Singh, P. S. Synthesis of novel silica-polyamide nanocomposite membrane with enhanced properties. *J. Membr. Sci. J.* **328**, 257–267 (2009).
2. Yin, J. & Deng, B. Polymer-matrix nanocomposite membranes for water treatment. *J. Memb. Sci.* **479**, 256–275 (2015).
3. Lenart, W. R. & Hore, M. J. A. Structure–property relationships of polymer-grafted nanospheres for designing advanced nanocomposites. *Nano-Structures and Nano-Objects* **16**, 428–440 (2018).
4. Yang, H., Pi, J., Liao, K., Huang, H., Wu, Q., Huang, X. & Xu, Z. Silica-Decorated Polypropylene Micro filtration Membranes with a Mussel-Inspired Intermediate Layer for Oil-in-Water Emulsion Separation. *ACS Appl. Mater. Interfaces* **6**, 12566–12572 (2014).
5. Kudilil, S., Kumbamala, S. & Joseph, R. Thermal and mechanical properties of polypropylene / titanium dioxide nanocomposite fibers. *Mater. Des.* **37**, 537–542 (2012).

6. Mina, F., Seema, S., Matin, R., Rahaman, J., Bijoy, R., Gafur, A. & Hashan, A. Improved performance of isotactic polypropylene / titanium dioxide composites : Effect of processing conditions and filler content. *Polym. Degrad. Stab.* **94**, 183–188 (2009).
7. Wang, J. F., Zhang, J. J. & He, D. N. Flower-like TiO<sub>2</sub>-B particles wrapped by graphene with different contents as an anode material for lithium-ion batteries. *Nano-Structures and Nano-Objects* **15**, 216–223 (2018).
8. Anbarasu, S., Ilangovan, S., Nagarethinam, V. S., Srivind, J., Balamurugan, S., Suganya, M. & Balu, A. R. Improvement in the visible light mediated photocatalytic activity of Al<sub>2</sub>O<sub>3</sub> nanoparticles through Zn<sup>2+</sup> doping. *Nano-Structures and Nano-Objects* **17**, 67–76 (2019).
9. Chouhan, S., Bajpai, A. K. & Bhatt, R. Analysis of topographical parameters and interfacial interaction of zinc oxide reinforced poly (vinyl alcohol-g-acrylonitrile) nanocomposite film surfaces using atomic force microscopy. *Nano-Structures and Nano-Objects* **18**, 100308 (2019).
10. Rohlmann, C. O., Horst, M. F., Quinzani, L. M. & Failla, M. D. Comparative analysis of nanocomposites based on polypropylene and different montmorillonites. *Eur. Polym. J.* **44**, 2749–2760 (2008).
11. Shawky, H. A., Chae, S., Lin, S. & Wiesner, M. R. Synthesis and characterization of a carbon nanotube / polymer nanocomposite membrane for water treatment. *DES* **272**, 46–50 (2011).
12. Costa, C. M., Rodrigues, L. C., Sencadas, V., Silva, M. M., Rocha, J. G. & Lanceros-méndez, S. Effect of degree of porosity on the properties of poly ( vinylidene fluoride – trifluoroethylene ) for Li-ion battery separators. *J. Memb. Sci.* **407–408**, 193–201 (2012).
13. Dey, S., Purahmad, M. & Ray, S. S. Investigation of PVDF-TrFE Nanofibers for Energy Harvesting. 21–24 (2012).
14. Prince, J. A., Singh, G., Rana, D., Matsuura, T., Anbharasi, V. & Shanmugasundaram, T. S. Preparation and characterization of highly hydrophobic poly ( vinylidene fluoride ) – Clay nanocomposite nanofiber membranes ( PVDF – clay NNMs ) for desalination using direct contact membrane distillation. *J. Memb. Sci.* **397–398**, 80–86 (2012).
15. Prasanth, R., Shubha, N., Hoon, H. & Srinivasan, M. Effect of nano-clay on ionic conductivity and electrochemical properties of poly ( vinylidene fluoride ) based nanocomposite porous polymer membranes and their application as polymer

- electrolyte in lithium ion batteries. *Eur. Polym. J.* **49**, 307–318 (2013).
16. Koh, M. J., Hwang, H. Y., Kim, D. J., Kim, H. J. & Hong, Y. T. Preparation and Characterization of Porous PVdF-HFP / clay Nanocomposite Membranes. *J. Mater. Sci. Technol.* **26**, 633–638 (2010).
  17. Bae, T., Kim, I. & Tak, T. Preparation and characterization of fouling-resistant TiO<sub>2</sub> self-assembled nanocomposite membranes. *J. Memb. Sci.* **275**, 1–5 (2006).
  18. Shui, Y., Yan, L., Bao, C. & Jiang, L. Treatment of oily wastewater by organic – inorganic composite tubular ultrafiltration ( UF ) membranes. *Desalination* **196**, 76–83 (2006).
  19. Mural, P. K. S., Sharma, M., Shukla, A., Bhadra, S., Padmanabhan, B., Madras, G. & Bose, S. RSC Advances Porous membranes designed from bi-phasic polymeric blends containing silver decorated reduced graphene oxide synthesized via a facile. *RSC Adv.* **5**, 32441–32451 (2015).
  20. Subramania, A., Sundaram, N. T. K., Priya, A. R. S. & Kumar, G. V. Preparation of a novel composite micro-porous polymer electrolyte membrane for high performance Li-ion battery. *J. Memb. Sci.* **294**, 8–15 (2007).
  21. Zhang, Q., Yang, H. & Fu, Q. Kinetics-controlled compatibilization of immiscible polypropylene / polystyrene blends using nano-SiO<sub>2</sub> particles. *Polymer (Guildf)*. **45**, 1913–1922 (2004).
  22. Kerakra, S., Bouhelal, S. & Ponçot, M. Study of Na-Montmorillonite-Polyamide Fiber/Polypropylene Hybrid Composite Prepared by Reactive Melt Mixing. *Int. J. Polym. Sci.* **2017**, 1–12 (2017).
  23. Arnal, M. L., Balsamo, V., Ronca, G., Sánchez, A., Müller, A. J., Cañizales, E. & Urbina De Navarro, C. Applications of Successive Self-Nucleation and Annealing (Ssa) To Polymer Characterization. *J. Therm. Anal. Calorim.* **59**, 451–470 (2000).
  24. Angulakshmi, N. & Stephan, A. M. Electrospun trilayer polymeric membranes as separator for lithium-ion batteries. *Electrochim. Acta* **127**, 167–172 (2014).
  25. Newman, A. & Kwok, D. *Contact angle measurement and contact angle interpretation. Adv. Colloid Interface Sci.* **81**, (1999).
  26. Jose, J. P., Abraham, J., Maria, H. J., Varughese, K. T. & Thomas, S. Contact Angle Studies in XLPE Hybrid Nanocomposites with Inorganic Nanofillers. *Macromol. Symp.* **366**, 66–78 (2016).
  27. Abraham, R., Varughese, K. T., Isac, J. & Thomas, S. Wetting properties of barium sodium niobate filled polystyrene nanocomposite. *Macromol. Symp.* **315**, 1–14 (2012).

28. Salzano De Luna, M. & Filippone, G. Effects of nanoparticles on the morphology of immiscible polymer blends - Challenges and opportunities. *Eur. Polym. J.* **79**, 198–218 (2016).
29. Taguet, A., Cassagnau, P. & Lopez-Cuesta, J. M. Structuration, selective dispersion and compatibilizing effect of (nano)fillers in polymer blends. *Prog. Polym. Sci.* **39**, 1526–1563 (2014).
30. Methakarn Jarnthong, Charoen Nakason, Natinee Lopattananon, Z. P. Influence of Incorporation Sequence of Silica Nanoparticles on Morphology, Crystallization Behavior, Mechanical Properties, and Thermal Resistance of Melt Blended Thermoplastic Natural Rubber. *Polym. Compos.* **33**, 1911–1920 (2012).
31. Bazgir, S., Katbab, a a & Nazockdast, H. Silica-Reinforced Dynamically Vulcanized Ethylene – Propylene – Diene Monomer / Polypropylene Thermoplastic Elastomers : Morphology , Rheology , and Dynamic Mechanical Properties. *J. Appl. Polym. Sci.* **92**, 2007 (2004).
32. Amin Mirzadeh, Pierre G. Lafleur, Musa R. Kamal, C. D. & Deuri, a S. The Effect of Compatibilizer on the Co-Continuity and Nanoclay Dispersion Level of TPE Nanocomposites Based on PP/EPDM. *Polym. Eng. Sci.* **50**, 2131–2142 (2010).
33. Jo, B., Park, S. & Kim, D. Mechanical properties of nano-MMT reinforced polymer composite and polymer concrete. *Constr. Build. Mater.* **22**, 14–20 (2008).
34. Kanny, K., Jawahar, P. & Moodley, V. K. Mechanical and tribological behavior of clay-polypropylene nanocomposites. *J. Mater. Sci.* **43**, 7230–7238 (2008).
35. Zhao, H. & Li, R. K. Y. Crystallization, mechanical, and fracture behaviors of spherical alumina-filled polypropylene nanocomposites. *J. Polym. Sci. Part B Polym. Phys.* **43**, 3652–3664 (2005).
36. Nguyen, V. G., Thai, H., Mai, D. H., Tran, H. T., Tran, D. L. & Vu, M. T. Effect of titanium dioxide on the properties of polyethylene/TiO<sub>2</sub> nanocomposites. *Compos. Part B Eng.* **45**, 1192–1198 (2013).
37. Esthappan, S. K., Kuttappan, S. K. & Joseph, R. Effect of titanium dioxide on the thermal ageing of polypropylene. *Polym. Degrad. Stab.* **97**, 615–620 (2012).
38. Ash, B. J., Rogers, D. F., Wiegand, C. J., Schadler, L. S., Siegel, R. W., Benicewicz, B. C. & Apple, T. O. M. Mechanical properties of Al<sub>2</sub>O<sub>3</sub>/polymethylmethacrylate nanocomposites. *Polym. Compos.* **23**, (2002).
39. Abad A Ares, M. J., Barral, L., Cano, J., Dez J Lpez, F. J. & Ramrez, C. Morphology and mechanical properties of polypropylene/organoclay nanocomposites. *J. Appl.*

- Polym. Sci.* **85**, 1562–1570 (2002).
40. Kuo, M. C., Huang, J. C. & Chen, M. Non-isothermal crystallization kinetic behavior of alumina nanoparticle filled poly(ether ether ketone). *Mater. Chem. Phys.* **99**, 258–268 (2006).
  41. K., B., Suriyakumar, S., P., A. P., A. S., A., Kalarikkal, N., Stephen, A. M., G., G. V., Rouxel, D. & Thomas, S. Highly lithium ion conductive, Al<sub>2</sub>O<sub>3</sub> decorated electrospun P(VDF-TrFE) membranes for lithium ion battery separators. *New J. Chem.* **42**, 19505–19520 (2018).
  42. Wang, S., Ajji, A., Guo, S. & Xiong, C. Preparation of microporous polypropylene/titanium dioxide composite membranes with enhanced electrolyte uptake capability via melt extruding and stretching. *Polymers (Basel)*. **9**, (2017).
  43. Sun, F., Li, T., Ren, H., Jiang, Q., Peng, H. & Lin, Q. PP/TiO<sub>2</sub> Melt-Blown Membranes for Oil/Water Separation and Photocatalysis: Manufacturing Techniques and Property Evaluations. *Polymers (Basel)*. **11**, 1–13 (2019).
  44. Salehi, M. M., Ataefard, M. & Moradian, S. The effect of nanoclay, PP and PP-g-MA type on properties of PP/clay nanocomposite: A way to investigate the dyeability mechanism. *Prog. Color. Color. Coatings* **10**, 73–84 (2017).
  45. Karacan, I. & Benli, H. An x-ray diffraction study for isotactic polypropylene fibres produced with take-up speeds of 2500-4250 M/Min. *Tekst. ve Konfeksiyon* **21**, 201–209 (2011).
  46. Bicy, K., Geethamma, V. G., Kalarikkal, N., Rouxel, D. & Thomas, S. Poly( $\epsilon$ -caprolactone)/Functionalized-Carbon Nanotube Electrospun Nanocomposites: Crystallization and Thermal Properties. *Macromol. Symp.* **381**, 1–6 (2018).
  47. Abdel-Hamid, H. M. Effect of electron beam irradiation on polypropylene films- dielectric and FT-IR studies. *Solid. State. Electron.* **49**, 1163–1167 (2005).
  48. Zhu, X., Yan, D. & Fang, Y. In Situ FTIR Spectroscopic Study of the Conformational Change of Isotactic Polypropylene during the Crystallization Process. *J. Phys. Chem. B* **105**, 12461–12463 (2001).
  49. Parthasarthy, G., Sevegney, M. & Kannan, R. M. Rheo-optical Fourier transform infrared spectroscopy of the deformation behavior in quenched and slow-cooled isotactic polypropylene films. *J. Polym. Sci. Part B Polym. Phys.* **40**, 2539–2551 (2002).
  50. Ensafi, A. A., Heydari-Bafrooei, E., Dinari, M. & Mallakpour, S. Improved immobilization of DNA to graphite surfaces, using amino acid modified clays. *J.*

- Mater. Chem. B* **2**, 3022 (2014).
51. Yu, J., Bai, H., Wang, J., Li, Z., Jiao, C., Liu, Q., Zhang, M. & Liu, L. Synthesis of aluminana nosheets via supercritical fluid technology with high uranyl adsorptive capacity. *New J. Chem.* **37**, 366–372 (2013).
  52. Rekha, M., Kathyayini, H. & Nagaraju, N. Catalytic activity of manganese oxide supported on alumina in the synthesis of quinoxalines. *Front. Chem. Sci. Eng.* **7**, 415–421 (2013).
  53. Skapski, A. S. The Temperature Coefficient of the Surface Tension of Liquid Metals. *J. Chem. Phys.* **16**, 386 (1948).
  54. Felix, J. M. & Gatenholm, P. The nature of adhesion in composites of modified cellulose fibers and polypropylene. *J. Appl. Polym. Sci.* **42**, 609–620 (1991).
  55. Li, D. & Neumann, A. Contact Angles On Hydrophobic Solid-surfaces And Their Interpretation. *J. Colloid Interface Sci.* **148**, 190–200 (1992).